ACS APPLIED BIO MATERIALS
Cite This: ACS Appl. Bio Mater. XXXX, XXX, XXX−XXX
Forum Article
www.acsabm.org

Amine-Functionalized MoO_3@RGO Nanohybrid-Based Biosensor for Breast Cancer Detection

Shine Augustine,[†] Pragati Kumar,[‡] and Bansi D. Malhotra*,[†]

[†]Nanobioelectronics Laboratory, Department of Biotechnology, Delhi Technological University, Delhi, 110042 India
[‡]Administrative Supervisor, Department of Electrical Engineering, Delhi Technological University, Delhi, 110042 India

Supporting Information

ABSTRACT: We report results of studies relating to development of an ultrasensitive, rapid, and label-free biosensor based on molybdenum trioxide (MoO_3) anchored onto the reduced graphene oxide (RGO) for breast cancer detection. The human epidermal growth factor receptor-2 (HER-2) secreted in the serum of breast cancer patients was used as an analyte for the detection. The *in situ* growth of 1D MoO_3 onto reduced graphene oxide (RGO), a 2D carbon substrate, was carried out via one-pot low-temperature hydrothermal synthesis. Subsequently, the surface conjugation of the monoclonal antibodies (anti-HER-2) onto the APTES/MoO_3@RGO/ITO electrode was conducted via EDC-NHS covalent chemistry. The structural and morphological properties of the MoO_3@RGO nanohybrid were investigated using electron microscopy, X-ray diffraction, scanning electron microscopy, transmission electron microscopy and X-ray photoelectron spectroscopic techniques. The surface area of the MoO_3@RGO nanohybrid determined via Brauner−Emmett−Teller analysis was found to be 14 times greater than that of the pristine MoO_3. The binding kinetics and the electrochemical activity of the developed platform were determined by cyclic voltammetry, differential pulse voltammetry, and impedance spectroscopic techniques. This nanohybrid based immunosensor exhibited improved sensitivity (13 uA $mLng^{-1}cm^{-2}$) in a broad concentration range (0.001−500 ng mL^{-1}) with a correlation coefficient of 0.98. The limit of detection of this MoO_3@RGO nanohybrid based immunosensor was found to be 0.001 ng mL^{-1}. The results obtained via the developed immunosensor for the quantification of serum HER-2 were validated using ELISA.

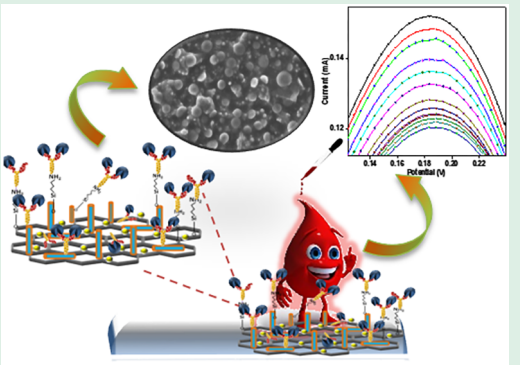

KEYWORDS: *molybdenum oxide, RGO, nanohybrid, label-free, HER-2, breast cancer*

INTRODUCTION

Transition metal oxides (TMOs)[1] have recently gained enormous interest because of their high surface activity, better catalytic efficiency, remarkable electrochemical properties, and variable oxidation states.[2] TMOs are composed of oxygen atoms bound to the transition metals leading to different physiochemical characteristics and polymorphism.[2] Among the various TMOs, molybdenum trioxide (MoO_3)[3] is a promising semiconductor material with a versatile stoichiometry, variable oxidation states (+2 to +6),[4] good catalytic activity, wide bandgap (>2.7 eV),[5] excellent electrical and surface charge properties,[6] and better biocompatibility.[7] Because of these unique characteristics, MoO_3 is being used for numerous applications including energy storage units, thermal materials, superconductors, electrochromic systems, and gas and biomedical sensors. In recent years, extensive efforts have been made toward the use of one-dimensional[8] (1D) MoO_3 because of their large surface- to-volume ratio, structural anisotropy,[9] and high electron mobility, improved surface scattering of electrons compared to that obtained in film and bulk form. In case of biosensing, the 1D morphology of MoO_3 is known to play a significant role by providing enhanced conjugation of desired biomolecules[10] due to the increased exposed surface area as compared to its nanoflakes, nanospheres, nanosheets, etc. Moreover, the polar nature and variable oxidation states facilitate improved binding of biomolecules and faster electron transfer, leading to better sensitivity. Enhanced loading of desired biomolecules onto a nanohybrid is crucial to obtain improved sensitivity of a biosensor. For instance, the incorporation of 1D MoO_3 onto a carbonaceous material results in increased electron and ionic mobility with enhanced kinetics.

Reduced graphene oxide (RGO) has emerged as an attractive two-dimensional (2D) carbonaceous material[11] because of its large specific surface area, high conductance, and high carrier mobility. Moreover, the ultrastability, and ease of functionalization with biomolecules[12] due to the reduced chemical groups makes it a potential material for biosensing. Many groups have reported the use of RGO and its nanocomposites with TMOs for

Special Issue: Biomaterials Research in India

Received: July 23, 2019
Accepted: September 6, 2019

DOI: 10.1021/acsabm.9b00659
ACS Appl. Bio Mater. XXXX, XXX, XXX−XXX

improved sensor characteristics. Zhou et al. synthesized the ZnO nanorods/RGO and used it for the fabrication of glucose biosensor and obtained a wide linear range.[13] In another study, OH et al. explored the role of nickel/RGO nanocomposite and found improved electrochemical performance of the designed electrode.[14] Verma et al. reported the application of Au@RGO matrix for oral cancer detection using IL-8.[15] Kumar et al. developed the ZrO_2@RGO based noninvasive immunosensor for oral cancer detection with improved sensitivity and limit of detection.[16] Chen et. al utilized Au@Ti loaded onto graphene nanosheets for immobilization of the given molecule for fabrication of the sandwich immunosensor. These reports revealed that hybrids with carbonaceous material[17] resulted in a sensitive and stable platform for biomedical sensing.[18,19]

Anchoring of MoO_3 (1D) onto the RGO (2D) is an effective strategy leading to better charge transfer ability, increased mechanical stability, and efficient heterogeneous electron activity[20] with improved surface area. RGO is an electroactive material with various active sites wherein the nucleation of MoO_3 results in the formation of nanorods[16] under hydrothermal conditions. MoO_3 perhaps prevents restacking of the RGO sheets, providing room for enhanced electron mobility by shuttling mechanism. Moreover, the abundant surface area of RGO aids in enhanced biomolecule loading[21] and the 1D morphology of MoO_3 with variable oxygen states facilitates better electron shuttling resulting in improved sensitivity and enhanced detection limit of the biosensor. Though some reports are available on the application of MoO_3@ RGO hybrid mainly in the area of supercapacitors, the potential of this hybrid remains unexplored in biosensing. In this study, we have tried to explore the potential of this nanohybrid in terms of electrochemical activity, conductivity, and the resulting biosensing performance. The timely detection of breast cancer biomarker is useful for both diagnostics and therapeutics, as it might reveal the presence of the disease.[22−24] Human epidermal growth factor receptor-2 (HER-2) has been considered as an important analyte for the diagnosis and prognosis of the disease.[23,25] HER-2 is a transmembrane protein comprising of tyrosine kinase receptor of 185 kDa and is cleaved into serum leading to the fluctuation in its level.[26] The normal level of HER-2 in serum[27] has been determined to be around ∼15 ng mL^{-1} and it rises to ∼75 ng mL^{-1} in the advanced cancer stage.[28,29] The current FDA approved technique for breast cancer detection includes immunohistochemistry (IHC) for analysis of HER-2 overexpression and fluorescence *in situ* hybridization (FISH) determining HER-2 gene amplification.[30] However, these techniques are largely laborious, require skilled personnel along with the need of advanced and sophisticated instrumentation with complex protocols, and are highly invasive (tissue samples).[31,32] Thus, the development of an ultrasensitive electrochemical immunosensor based on MoO_3@RGO nanohybrid is a new approach for quantifying the HER-2 levels in serum. This technique may perhaps overcome the current limitations, with numerous advantages such as ease of use, faster response, and minimal invasion, and holds potential for miniaturization. Numerous studies have been reported on the development of biosensors toward the detection of breast cancer (Table 2) that demonstrate the usefulness of HER-2.[33−35] However, these works suffer from being complex and have poor linear range, lower detection limit, and reduced sensitivity.

This paper deals with the development of an ultrasensitive label-free, rapid biosensor based on a new hybrid matrix (MoO_3@RGO) for the detection of HER-2 antigen secreted in the serums of breast cancer patients. The synthesized nanohybrid was characterized using XRD, SEM, TEM, BET, and XPS. The MoO_3@RGO nanohybrid was immobilized with a simple and effective strategy, i.e., monoclonal anti-HER-2 via covalent coupling reaction mechanism. This nanohybrid based immunosensor was used to estimate HER-2 in samples of patients.

EXPERIMENTAL SECTION

Chemicals. Sodium monophosphate [NaH_2PO_4], sodium diphosphatedihydrate [$Na_2HPO_4{\cdot}2H_2O$], potassium ferricyanide (K_3[Fe(CN)$_6$]), potassium ferrocyanide (K_4[Fe(CN)$_6$]3H_2O), and *N*-hydroxysuccinimide (NHS) [$C_4H_5NO_3$] were procured from Fisher Scientific. L-Cysteine ($C_3H_7NO_2S$) and sodium chloride [NaCl], were purchased from Himedia. Sodium molybdenum oxide dihydrate ($Na_2MoO_4{\cdot}2H_2O$) and 3-aminopropyltriethoxysilane (APTES) were from Alfa-Aesar. All of the analytical-grade chemicals were used without purification. Phosphate buffered saline (PBS) solution of pH 7.0 using $Na_2HPO_4{\cdot}2H_2O$ (0.05 mol L^{-1}) and NaH_2PO_4 (0.05 mol L^{-1}) was freshly prepared in Milli-Q water (18 MΩ cm^{-1}) and stored at 4 °C for desired experiments.

Instrumentation. The crystallinity and phase analysis were undertaken using X-ray diffractometer [Bruker D-8 Advance] with Cu−Kα radiation (λ = 1.5406 Å). The structural and morphological studies were observed through scanning electron microscope (SEM, Hitachi SN-3700) and transmission electron microscope (TEM, JEOL-JEM-2100F). The X-ray photoemission spectroscopy (XPS) investigations were conducted via K Alpha X-ray photoelectron spectrometer (Thermo Scientific) consisting of a monochromatized Al−Kα line centered at 1486.7 eV, operating with a base pressure of 3.75×10^{-9} Torr at 300 K. The instrument had an X-ray spot size of 400 μm with resolution of >25 meV and a constant analyzer energy (CAE) with lens in standard mode was also used. The wide survey scan and high-resolution core level spectra were fixed at 200 and 50 eV with step size of 0.1 eV. The Fourier transform infrared spectrometer (FT-IR) [PerkinElmer, Spectrum BX II was utilized to investigate the functional groups and bonds present in APTES/MoO_3@RGO/ITO and anti-HER-2/APTES/MoO_3@RGO/ITO. All the electrochemical studies were performed via a PGSTAT 302 N (Auto lab, Potentiostat Netherlands). All the electrochemical characterization experiments were performed via a three-electrode system consisting of working electrode (modified ITO-coated glass electrode), Ag/AgCl as a reference electrode and platinum (Pt) as a counter electrode. Phosphate buffer solution (PBS) (50 mM, 0.9% NaCl) of pH 7.0 was used as an electrolyte, consisting of 5 mM of ferro-ferri cyanide [Fe(CN)$_6^{3-/4-}$] as a redox couple. The HER-2 concentration in the serum sample (breast cancer patients) was determined using ELISA plate reader [Bio-Rad, Model 680]. To calculate the error bars, all measurements were performed in triplicate, and the error bars indicated one standard deviation about the mean value.

***In Situ* Synthesis of MoO_3@RGO Nanohybrid via the Hydrothermal Method.** A facile *in situ* synthesis was introduced for the formation of 1D MoO_3 onto a 2D carbon substrate, i.e., reduced GO (graphene oxide) nanohybrid using one low pot temperature hydrothermal method. The solution A was prepared by dispersing a certain amount of GO in (20 mL) of deionized water (DI) followed by ultrasonication for 3 h to exfoliate the stacked GO sheets. Simultaneously, the aqueous solution B was prepared by mixing 1.4 g of $Na_2MoO_4{\cdot}2H_2O$ in 20 mL of DI. Solutions A and B were mixed and gently stirred for 30 min at 250 rpm to get a stable suspension. Subsequently, 3 mL of HCl (6 M) was added to the above mixture to adjust the pH of resultant solution. The final solution mixture was then transferred to an autoclaved vessel (100 mL) and kept at 160 °C for 3 h. Finally, the subsequent homogeneous dispersion was centrifuged at 10 000 rpm and washed with Milli-Q water dried at 60 °C for 12 h. The obtained greyish black product was collected and stored at room temperature (RT-25 °C) until further use. The same procedure was followed for the synthesis of pristine MoO_3 in the absence of GO.

DOI: 10.1021/acsabm.9b00659
ACS Appl. Bio Mater. XXXX, XXX, XXX−XXX

Scheme 1. Pictorial Representation of Development of Immunoelectrode for Breast Cancer Biomarker Detection

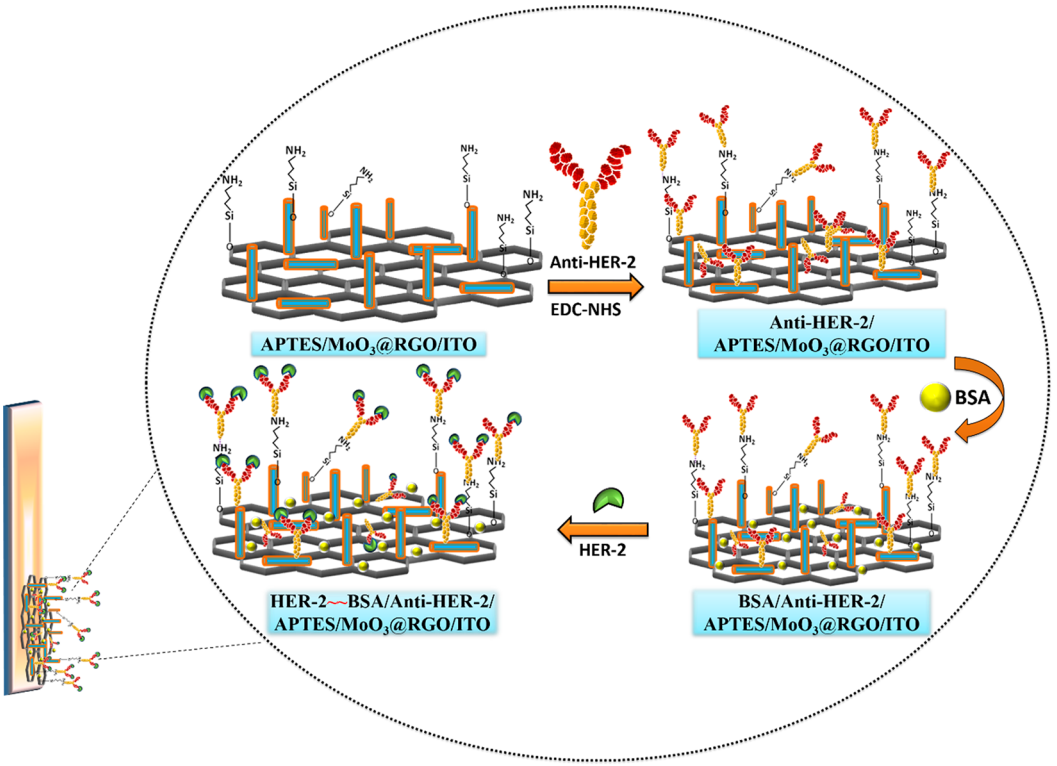

Amine Functionalization of MoO_3@RGO Nanohybrid with a Linker Molecule. The bioconjugation of a protein biomolecule to the nanocomposite was facilitated using a linker molecule for the fabrication of efficient biosensing platform. The silane coupling agent such as (3-aminopropyl) triethoxysilane (APTES) possesses inorganic and an organic end. The primary amine group at one end and silane reactive hydrolyzable group on another end that gets attached to the matrix surface, making APTES a potential linker agent.[36] In the present study, the surface treatment of as-synthesized MoO_3@RGO nanohybrids was performed using APTES. For this, a homogeneous mixture of MoO_3@RGO nanohybrid was prepared (200 mg in 10 mL of isopropyl alcohol (IPA)) and stirred at 300 rpm for 2 h at 40 °C. Two hundred microliters of APTES was introduced to the above solution dropwise under continuous stirring for the next 1 h. Subsequently, DI (5 mL) water was added to the above solution for complete hydrolysis of APTES. The whole mixture was left for 48 h at constant stirring (300 rpm). During the salinization process, the APTES molecules underwent chemical modification, wherein the triethoxyl groups ($(OC_2H_5)_3$-Si-$(CH_2)_3NH_2$) got converted into trihydroxyl groups ($(OH)_3$-Si-$(CH_2)_3NH_2$) followed by polycondensation of the hydroxyl group with the hydroxyl group onto the MoO_3@RGO nanohybrid surface. This free amine terminal of APTES was further utilized for covalent attachment of biomolecules to the nanohybrid surface. The functionalized nanohybrid was centrifugated (10 000 rpm, 20 min) and washed with DI followed by drying at 65 °C in a hot air oven.

Electrode Fabrication. The electrophoretic deposition (EPD) technique was used to deposit the amine functionalized (APTES/MoO_3@RGO) nanohybrid onto a conductive glass substrate coated with indium tin oxide (ITO). Initially, a homogeneous colloidal suspension of APTES/MoO_3@RGO nanohybrids (1 $mgmL^{-1}$) in acetonitrile was prepared by ultra- sonication (40W, 0.25 A) for about 2 h. Prior to this, the ITO was hydrolyzed with NH_3:H_2O_2: H_2O in a 1:1:5 ratio to introduce the hydroxyl group onto its surface. For EPD, 10 mL of this stock solution was introduced into a two-electrode glass cell consisting of working electrode (ITO) and platinum (Pt) as a counter electrode. Charger salt (1×10^{-5} to 1×10^{-4} mol of Mg $(NO_3)_2 \cdot 6H_2O$) was introduced in the electrolyte to introduce a surface charge on APTES/MoO_3@RGO nanohybrids and fabricate a uniform thin film on the ITO electrode. On applying the external electric field (50 V DC for 2 min), a uniform thin film was obtained at the ITO surface (size, 0.25 cm^2). The Mg^{2+} ions were absorbed by the nanohybrid, providing a sufficient positive charge and resulting in an enriched deposition at the anode (ITO). Subsequently, the fabricated electrodes (APTES/MoO_3@RGO/ITO) were removed and stored at RT (25 °C) until further usage.

Fabrication of MoO_3@RGO Nanohybrid-Based Immunosensor. For immunosensor fabrication, a stock solution of antibodies (anti-HER-2, 50 $\mu g\ mL^{-1}$) prepared in PBS (pH 7.0) was used. Prior to the biomolecule immobilization, EDC-NHS coupling chemistry was utilized to activate the −COOH groups of antibodies. A mixture of the solution in a 2:1:1 ration of anti-HER-2, EDC, and NHS was prepared wherein NHS (0.05 M) was employed as an activator and EDC (0.2 M) as a coupling agent kept at RT (25 °C) for 30 min. Further, the activated antibody solution (30 μL) was drop cast onto the surface of APTES/MoO_3@RGO/ITO electrode. These electrodes were kept in a humid environment for about 5 h and stored at 4 °C.

Scheme 1 represents the tentative binding of anti-HER-2 onto the proposed immunoelectrode. To remove any unbound antibody molecules, these anti-HER-2/APTES/MoO_3@RGO/ITO electrodes were washed thoroughly with PBS (pH 7.0). It should be noted that the amine groups ($-NH_2$) of functionalized nanohybrids got covalently attached to the activated carboxylic group (−COOH) of anti- HER-2 resulting in amide bond (C−N) formation. Finally, the bovine serum albumin (20 μL, 1 $mgdL^{-1}$) was spread on the surface of immunoelectrode (anti-HER-2/APTES/MoO_3@RGO/ITO) to block the nonspecific active sites of the prepared bio electrode. The as-prepared immunoelectrode (BSA/anti-HER-2/APTES/MoO_3@RGO/ITO) was washed with PBS (pH 7.0) and stored at 4 °C until further use.

RESULTS AND DISCUSSION

XRD Studies. Figure 1 depicts the XRD (copper K_α radiation) pattern of the as-prepared MoO_3@ RGO nanohybrid and pristine MoO_3 in the range, 10−80° at a scan rate of 0.2° min. The peaks found at 2Θ = 12.8, 23.5, 25.8, 27.4, 35.2, and

DOI: 10.1021/acsabm.9b00659
ACS Appl. Bio Mater. XXXX, XXX, XXX−XXX

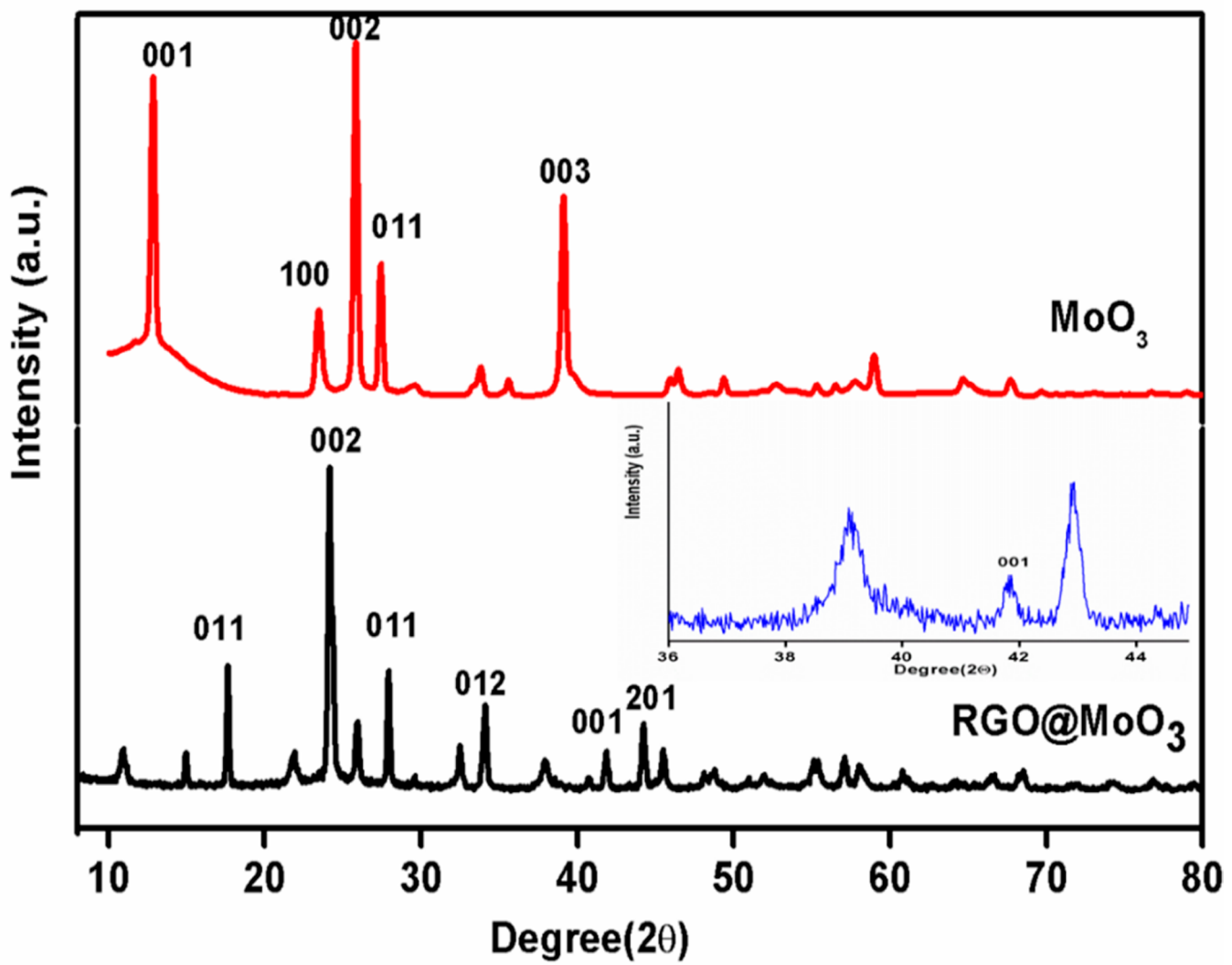

Figure 1. X-ray diffraction of $MoO_3$and MoO_3@RGO nanohybrid.

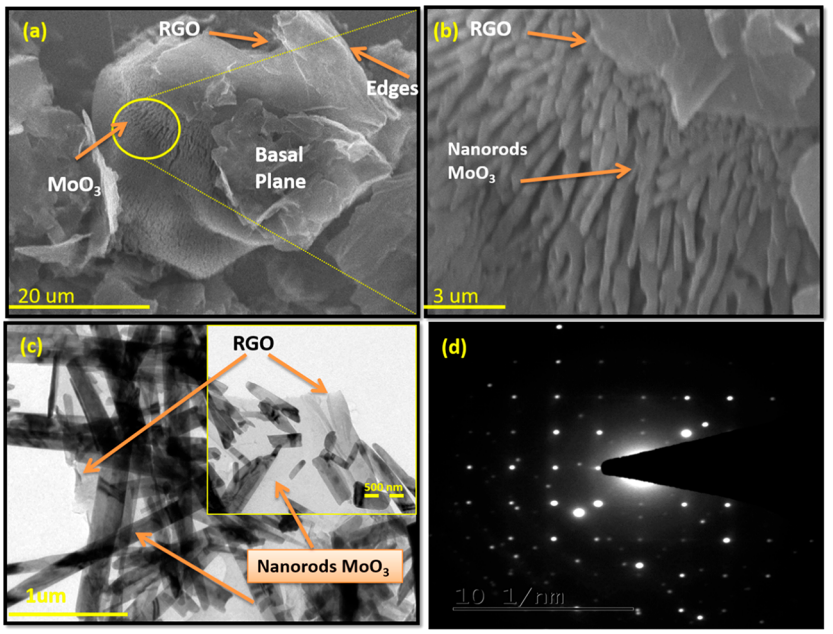

Figure 2. (a, b) SEM, (c) TEM, and (d) SAED pattern of MoO_3@RGO nanohybrid.

DOI: 10.1021/acsabm.9b00659
ACS Appl. Bio Mater. XXXX, XXX, XXX−XXX

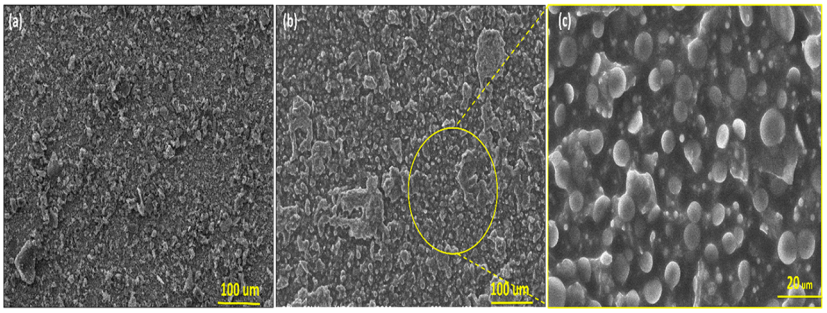

Figure 3. SEM images of (a) APTES/MoO_3@RGO/ITO and (b, c) anti-HER-2 attached to the APTES/MoO_3@RGO/ITO electrode.

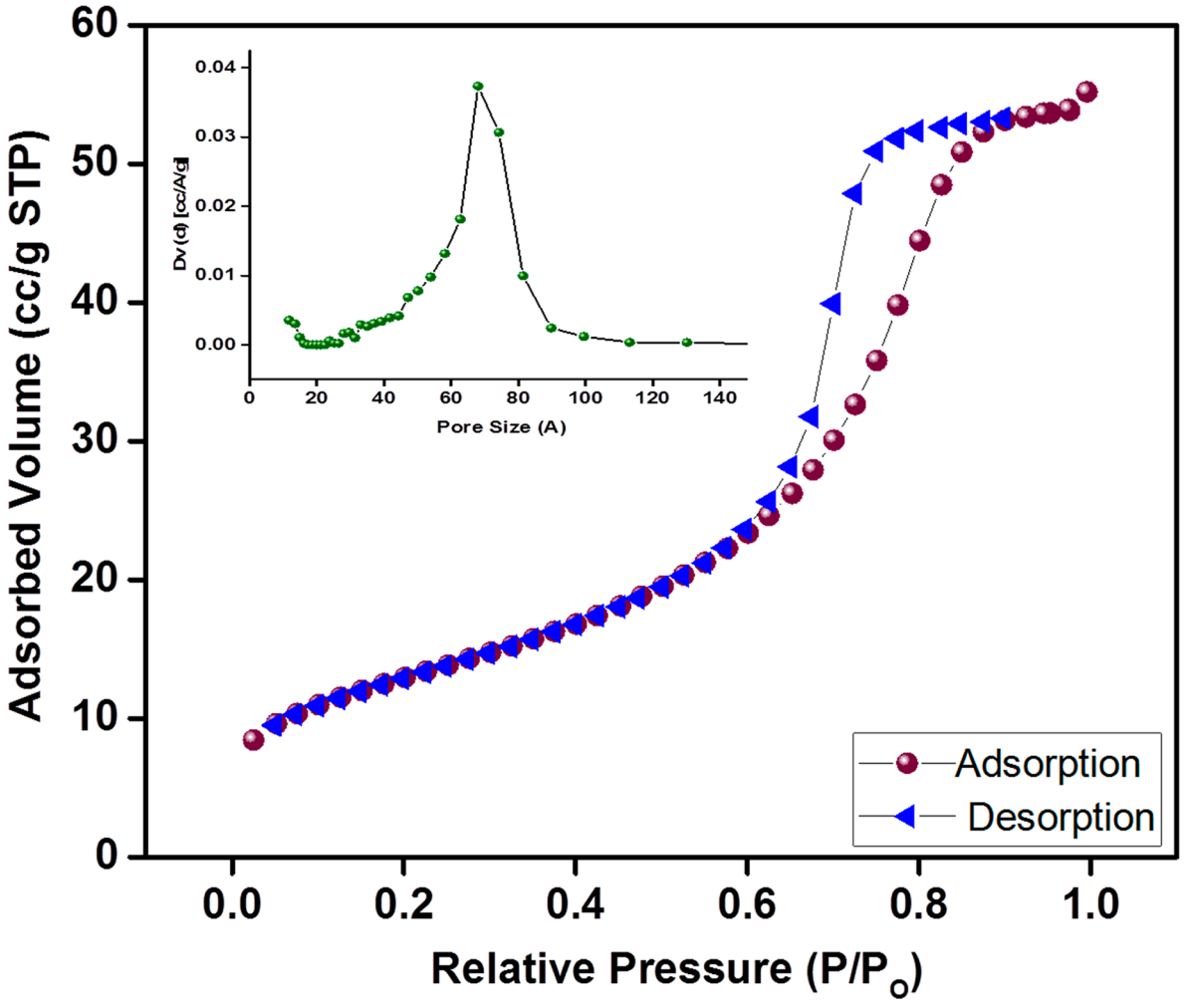

Figure 4. BET analysis of MoO_3@ RGO nanohybrid.

39.1° were indexed to the characteristic *hkl* planes of MoO_3 at (001), (100), (002), (011), (012), and (003) (Figure 1), corresponding to the orthogonal structure of MoO_3 with the lattice parameters (a = 3.95, b = 3.68, and c = 7.09) (JCPDS card No. 15−1621). The highest intensity observed at 2θ = 25.83° at the plane (002) revealed that MoO_3 crystallites grew more orderly along the (002) plane. Further, in the nanohybrid, lower intensity broad peak observed at 43.0° indicated the presence of RGO in the (001) plane, suggesting disordered stacking and reduced agglomeration of the sheets in the composite.[37] The highly crystalline behavior observed in the XRD pattern of pristine MoO_3 and MoO_3@RGO nanohybrids suggested that the MoO_3 nanorods were densely grown on the RGO sheet with reduced interlayer stacking in the composite.[20]

Microscopic Studies. The structural and morphological studies were performed via SEM and TEM techniques. Figure 2a, b depicts the SEM image in low magnification of the synthesized MoO_3@RGO nanohybrid. In Figure 2a, the randomly anchored MoO_3 nanorods on the rough textured RGO sheets can be seen. The growth of nanorods onto the electro-active sites of 2D RGO sheet in a random manner was perhaps due to availability of the oxygen groups on the RGO surface that were found to form a network structure (Figure 2b) highlighted by a yellow circle. Figure 2c shows TEM images of the synthesized nanohybrid, prepared ultrasonically by dispers-

DOI: 10.1021/acsabm.9b00659
ACS Appl. Bio Mater. XXXX, XXX, XXX−XXX

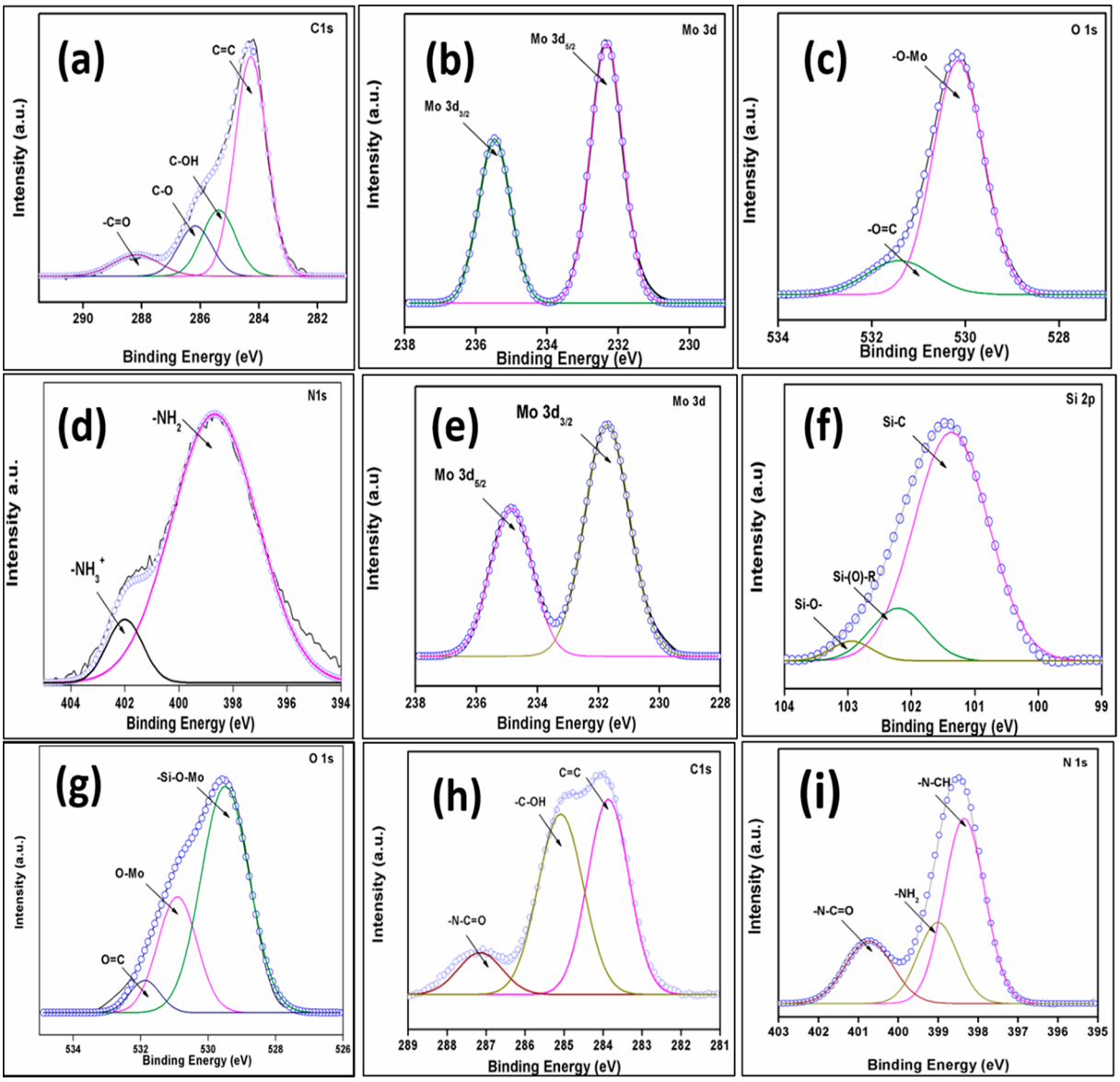

Figure 5. Deconvoluted spectra of (a–c) C 1s, Mo 3d, and O 1s in MoO_3@RGO/ITO; (d–g) N 1s, Mo 3d, Si 2p, and O 1s in APTES/MoO_3@RGO/ITO; (h–i) C 1s and N 1s in anti-HER-2/APTES/MoO_3@RGO/ITO.

ing in ethanol and subsequently placing it on a copper grid via drop cast and air-drying. The morphology and structure of the MoO_3@RGO nanohybrid (Figure 2c) were in agreement with the results of SEM studies. The thin sheet structure of RGO acted as the hydrophilic base for growing nanorods of MoO_3 in bundles. The width of the MoO_3 nanorod was estimated to be 40–50 nm. The light, thin sheet structure was ascribed to the presence of RGO, whereas the rod like structures confirmed the presence of MoO_3 intertwined with RGO. The selected area electron diffraction (SAED) pattern of the MoO_3@RGO nanohybrid (Figure 2d) corresponded to the planes of MoO_3 depicting the orthorhombic phase as shown by the XRD data.

The SEM image of the APTES/MoO_3@RGO/ITO electrode pre- and post-immobilization of anti-HER-2 is shown in Figure 3a–c. The modification in the surface morphology after the antibody immobilization is clearly visible in Figure 3b, c because the rough surface of the APTES-modified electrode was perhaps transformed to a smoother surface. The globular morphology seen in Figure 3c demonstrated the presence of antibodies attached to the APTES/MoO_3@RGO/ITO electrode.

Brauner–Emmett–Teller Measurements. The porosity of synthesized MoO_3@ RGO and MoO_3, was investigated via Brauner–Emmett–Teller (BET) measurements.[38] The specific surface area was sampled by degassing the nanomaterial in vacuum at 200 °C for 8 h followed by the nitrogen adsorption, and desorption isotherms measurements. (Figure 4). The Barrett–Joyner–Halenda (BJH) method was used for analyzing the specific surface area and pore size distribution. The total BET surface area and average pore diameter for MoO_3@RGO (Figure 4 (inset)) were found to be 2.58×10^2 m^2 g^{-1} and 8.4 nm. The surface area in this hybrid was found to be 14 times greater than that of pristine MoO_3 (17.19 m^2 g^{-1}) and the pore size was enhanced 4 times.[38] The estimated pore volume from the adsorbed nitrogen gas at a relative pressure (P/P_o) of 0.994 at temperature of 77.35 K was found to be 8.78×10^{-1} cc g^{-1}. The results of this study revealed that anchoring of MoO_3 nanorods onto a 2D RGO substrate resulted in the improved

DOI: 10.1021/acsabm.9b00659
ACS Appl. Bio Mater. XXXX, XXX, XXX–XXX

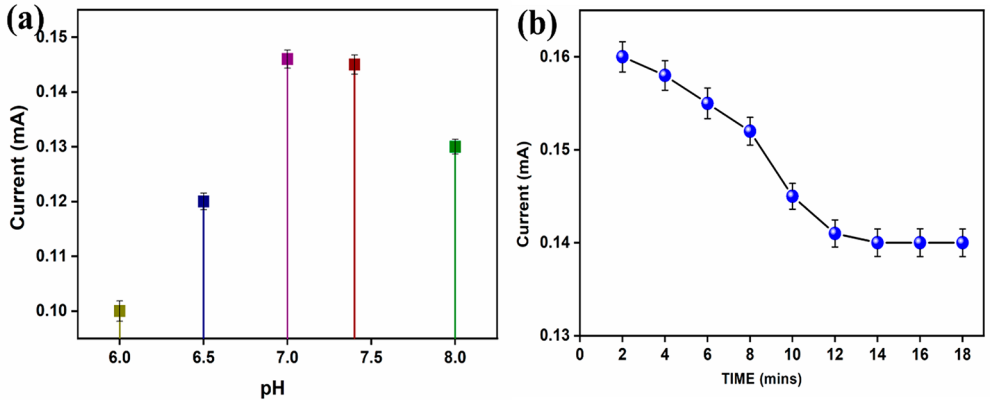

Figure 6. (a) Effect of pH, (b) incubation time study of BSA/anti-HER-2/APTES/MoO_3@RGO/ITO immunoelectrode.

surface area, leading to mesoporous structure. This enhancement in the surface area resulted in the mesoporic behavior of this nanohybrid accelerated the charge transfer and increased the loading of the biomolecules.[10]

FT-IR Studies. The Fourier transform infrared spectra (FT-IR) of APTES/MoO_3@RGO/ITO and anti-HER-2/APTES/MoO_3@ RGO were obtained in the range, 400−4000 cm^{-1} (Figure S1). The peak present in curves a and b seen at around 1110 cm^{-1} was attributed to the Si−O bonding of the APTES with the synthesized MoO_3@RGO. The peaks present at 780 and 990 cm^{-1} for the as-prepared APTES/MoO_3@RGO were assigned to asymmetric and symmetric stretching of Mo−O of MoO_3.[39] The peak found at 990 cm^{-1} was due to the terminal Mo═O bond in the orthorhombic phase, indicating good correlation with XRD data.[3] The peak seen at 870 cm^{-1} was due to the Mo−O−Mo vibrations of Mo^{6+}, indicating good agreement with XPS studies. Further, in curve b, −OH and −N−H stretching vibrations of water molecules are depicted by the band present at 3300 cm^{-1}. The peak seen at 1527 cm^{-1} corresponded to the amide II band and −C═O stretching formed between the NH_2 present on the APTES/MoO_3@ RGO and the −COOH group of the anti-HER-2, confirming the attachment of antibodies to the functionalized nanohybrid.[16,17]

XPS Studies. The XPS studies were conducted to investigate the composition and valence states of the elements present in the MoO_3@RGO, APTES/MoO_3@RGO/ITO, and anti-HER-2/APTES/MoO_3@RGO/ITO. The survey scan spectrum (Figure S4) confirmed the presence of C 1s (284.5), N 1s(399.6 eV), O 1s (530.5 eV), Si 2p (102.0 eV), and Mo 3d (232.0 eV) at their respective binding energies. All the obtained spectra were adjusted to C 1s peak at 284.5 eV. The XPS spectra of the elements Mo 3d, O 1s, C 1s, N 1s, and Si 2p were deconvoluted to their corresponding binding energies, as shown in Figure 5a−h. The C 1s spectra of RGO in MoO_3@RGO/ITO was deconvoluted to four distinct peaks (Figure 5a), each corresponding to the presence of functional groups i.e. at 284.5 eV (C═C) of carbon sp^2, C−C at 285.3 eV, −C−O at 286.1 eV of epoxy/hydroxyl, and −O−C═O at 288.1 eV of carboxylates.[40] The Mo 3d spectrum (Figure 5b) exhibited two spin−orbit peaks at 232.5 and 235.6 eV relating to Mo $3d_{5/2}$ and Mo $3d_{3/2}$ in the +6 state with the spin−orbital splitting at 3.1 eV.[29] After functionalization with the APTES, the peaks were found to shift to 231.7 and 234.8 eV, corresponding to the Mo $3d_{5/2}$ and Mo $3d_{3/2}$ in the +5-state attributed to the surface oxidation (Figure 5e). Figure 5c shows the presence of O 1s before salinization with APTES. The deconvoluted peaks at 530.1 and 531.4 eV corresponded to oxygen linked to molybdenum (−O−Mo−) and oxygen double bonded to carbon (−O═C), respectively.[41] In the case of the APTES/MoO_3@RGO/ITO (Figure 5d−f), the presence of Si 2p and N 1s confirmed the salinization. The N 1s peaks observed after APTES treatment were deconvoluted into two peaks at 398.6 and 401.9 eV corresponding to −**N**−CH and $-NH^{+3}$, respectively (Figure 5d). Further, the spectra of Si 2p (Figure 5f) was deconvoluted to their respective binding energies. The peaks seen at 101.3, 102.1, and 103.2 eV corresponded to −Si−C−, Si−(O)−Mo, and −Si−O−.[42] The contribution of these peaks confirmed amine functionalization of the synthesized MoO_3@RGO nanohybrid with APTES. Further, the deconvoluted peak of O 1s in the range 529−531 eV was observed post-APTES functionalization at 529.4, 530.9, and 531.9 eV.[43] The highest peak found at 529.4 eV was assigned to the formation of −Si−O−Mo bond in the (Figure 5g) MoO_3@RGO nanohybrid. Figure 5h, I shows the deconvoluted peaks of C 1s and N 1s post immobilization with anti-HER-2 immobilized onto APTES/MoO_3@RGO/ITO electrode. The C 1s peaks were deconvoluted to three peaks at 283.4, 285.0, and 287.1 eV. The peak at 287.1 corresponded to carbon linked to the amide bond formation (−N−C═O). Further, the deconvoluted peaks of N 1s appearing at 398.0, 399, and 400.7 eV corresponded to the nitrogen of the amide bond formed between −N═C−O (400.7 eV)[30] and primary amine ($-NH_2$) of antibody (399.0 eV). The results of these XPS studies confirmed the modification of electrodes at every step.

Electrochemical Studies. Electrochemical characteristics were determined via cyclic voltammetry (CV), differential pulse voltammetry (DPV) and electron impedance spectroscopy (EIS) during the fabrication of HER-2 immunosensor. The PBS (50 mM, pH 7.0) consisting of 5 mM Fe $(CN)_6^{4-}$ (ferrocyanide), 5 mM of Fe $(CN)_6^{3-}$ (ferricyanide) and 0.9% NaCl as a redox mediator was used throughout the experiments, for monitoring electron transfer between the fabricated electrodes and the electrolyte. The electrons generated during the electrochemical reaction were facilitated via the Fe (III)/Fe (IV) redox agent resulting in a current signal revealing the unique role of the fabricated electrode. This redox couple exhibited a heterogeneous one-electron transfer (n = 1). DPV was utilized for measuring the response of the immunosensor because it generated a peak about the faradic current only.

Effect of pH. Extreme pH is known to induce conformational changes in the biomolecule leading to the hindered antibody and antigen interaction.[44] Thus, prior to the

DOI: 10.1021/acsabm.9b00659
ACS Appl. Bio Mater. XXXX, XXX, XXX−XXX

electrochemical experiments effect of pH was determined to explore the electrochemical response of the anti-HER-2 present in the fabricated immunoelectrode. Here, the PBS (50 mM, 0.9% NaCl) of different pH (6.0−8.0) containing 5 mM of $[(Fe(CN)_6)]^{3-/4-}$ ions using DPV. These results showed that with increasing pH, the magnitude of current response of the immunosensor increased and the maximum peak current response was obtained at pH 7.0 (Figure 6a). This increase in current was due to the fact that, at neutral pH, the anti-HER-2 existed in its natural form and exhibited the highest activity. Nevertheless, in case of an increase or decrease beyond pH 7.0 the biomolecules tended to denature and lose their natural activity because of interaction between H^+ or OH^- ions present in the buffer.[45] Thus, pH 7.0 was used throughout the electrochemical experiments.

Incubation Studies. The duration of the time of interaction of antigen and antibody was investigated via the DPV technique. Here, the interaction time between the HER-2 antigen and anti-HER-2 present in BSA/anti-HER-2/APTES/nMoO_3/ITO electrode was recorded via the DPV technique at regular intervals of 25 min with a fixed antigen concentration (1 $ngmL^{-1}$). The obtained results (Figure 6b) clearly showed that 15 min was the maximum time required for complete interaction, after which the current response abruptly changed.

Scan Rate Studies. The cyclic voltammetry studies were performed to investigate the interfacial kinetics and the redox property of the modified electrodes. Figures S2 and S3 shows the cyclic voltammograms recorded for APTES/MoO_3@RGO/ITO and BSA/anti-HER-2/APTES/MoO_3@RGO/ITO electrodes at varying scan rate from 40 to 160 mVs^{-1}. In both the electrodes, with the increasing scan rate, a positive shift of the oxidation peak and a negative shift of the reduction peak was observed.[46] Moreover, the peak-to-peak separation voltage of electrodes increased and shifted toward the higher potential side at increasing scan rates, resulting in reversible electron transfer kinetics of the electrode.[47] According to the Randle−Sevick equation, a linear relation was observed with the magnitude of peak currents of both the electrodes vs square root of scan rate ($v^{1/2}$) (inset i of Figures S2 and S3). This result indicated that the reaction was governed by diffusion assisted electron transfer[48] mechanism and calculated using the linear curve fitting given by (eqs 1−4)

$$I_{pa(APTES/MoO3@RGO/ITO))} = [6 \times 10^{-5}(s/mV) + 1.4 \times 10^{-4}(\text{scan rate}[mV/s])^{1/2}]\ R^2 = 0.996,\ SD = 1.6 \times 10^{-5} \quad (1)$$

$$I_{pc(APTES/MoO3@RGO/ITO))} = [-4.13 \times 10^{-5}(s/mV) - 1.5 \times 10^{-4}(\text{scan rate}[mV/s])^{1/2}]\ R^2 = 0.996,\ SD = 5.8 \times 10^{-4} \quad (2)$$

$$I_{pa((BSA/anti-HER-2/APTES/MoO3@RGO/ITO)} = [5.2 \times 10^{-5}(s/mV) + 7.7 \times 10^{-7}(\text{scan rate}[mV/s])^{1/2}]\ R^2 = 0.996,\ SD = 7.3 \times 10^{-6} \quad (3)$$

$$I_{pc(BSA/anti-HER-2/APTES/MoO3@RGO\ ITO)} = [-4.14 \times 10^{-5}(s/mV) - 1.34 \times 10^{-4}(\text{scan rate}[mV/s])^{1/2}]\ R^2 = 0.997,\ SD = 3.4 \times 10^{-4} \quad (4)$$

The value of ΔEp was found to be linear with increasing scan rate indicating that the kinetics showed quasi-reversible behavior suggesting that the rate of mass transport was almost equal to the rate of electron transfer (Figures S2 and S3, inset ii).[49]

Electrode Studies. Electrode studies were performed to monitor the effect of modification of the electrode at the various steps. Figure 7 shows the DPV response of (i) ITO, (ii) APTES/MoO_3/ITO, (iii) APTES/RGO/ITO, (iv) APTES/MoO_3@RGO/ITO, (v) anti-HER-2/APTES/MoO_3@RGO/ITO, and (vi) BSA/anti-HER-2/APTES/MoO_3@RGO/ITO electrodes at a scan rate of 50 mVs^{-1} in the potential range −0.2 to +0.6 V. The magnitude of electrochemical current for the bare hydrolyzed ITO was found to be ∼0.13 mA. The magnitude of the peak current obtained for the APTES/MoO_3/ITO and APTES/RGO/ITO electrode was found to be 0.11 and 0.12 mA, respectively. After electrophoretic deposition of the APTES/MoO_3@RGO onto the hydrolyzed ITO electrode, the magnitude of electrochemical current was found to increase by about 1.6 times ∼0.22 mA, with respect to MoO_3 and RGO respectively. It could be due to grafting of 1D MoO_3 nanorods onto the 2D RGO sheets leading to better electron conduction pathway for transfer from bulk electrolyte solution toward the ITO electrode.[50] In addition to this, the presence of edgelike defective sites in RGO nanosheets accelerated the charge transfer process at the electrode solution interface.[51] In an earlier study, Huang et al. demonstrated the synthesis of NiO/RGO composite toward the high-performance glucose biosensing.[52] Here the incorporation of NiO into the RGO matrix resulted in the enhancement of electrochemical current. Kumar et al. observed that the incorporation of the zirconium oxide onto reduced graphene oxide, led to its enhanced electrochemical properties and faster and reversible redox reactivity.[16] As anticipated, after the modification of APTES/MoO_3@RGO/ITO surface with anti-HER-2, the peak current (0.19 mA) slightly decreased . The presence of the macromolecular layer of antibodies on the nanohybrid matrix exhibited insulating characteristics and acted as a hindrance to the fast electron

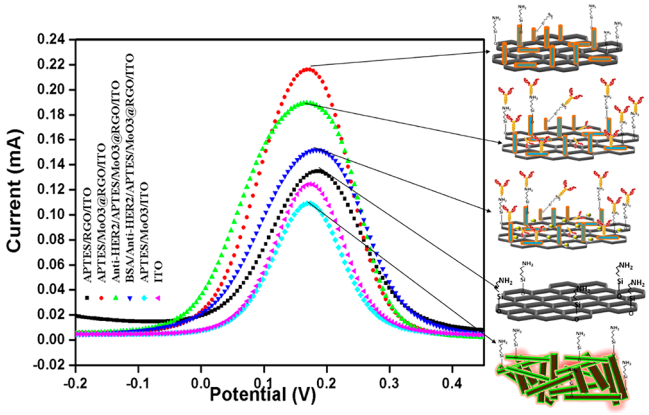

Figure 7. Electrochemical peak response obtained via DPV at each step of electrode modification.

DOI: 10.1021/acsabm.9b00659
ACS Appl. Bio Mater. XXXX, XXX, XXX−XXX

transfer kinectics.[53] These studies also confirmed the attachment of antibodies on this mesoporous composite, leading to reduced electron transfer.[54] The peak current (0.145 mA) further decreased after BSA immobilization onto the anti-HER-2/APTES/MoO_3@RGO/ITO, confirming the blocking of the non-specific binding site at the electrode surface.

The variation in diffusion coefficient (D) determined using Randle−Sevick at each modification step (ITO, APTES/MoO_3/ITO, APTES/RGO/ITO, APTES/MoO_3@RGO/ITO, anti-HER-2/APTES/MoO_3@RGO/ITO, and BSA/anti-HER-2/APTES/MoO_3@RGO/ITO electrodes) at the interface of the redox species $[(Fe(CN)_6)]^{3-/4}$ followed eq 5:

$$I_p = (2.69 \times 10^5) n^{3/2} A D^{1/2} C \nu^{1/2} \quad (5)$$

Where I_p is the peak current of immunoelectrode, D is the diffusion coefficient, n is the number of electrons (1) transferred, C is the concentration of redox species (5×10^{-3} mol cm^{-2}), A is the active surface area of the electrode (0.25 cm^2), and υ is the scan rate (50 mV/s). The D value (Table 1) is found to be

Table 1. Diffusion Coefficient of the Modified Electrodes

electrode	diffusion coefficient ($cm^2\ s^{-1}$)[a]
ITO	3.06×10^{-12}
APTES/MoO_3/ITO	1.96×10^{-12}
APTES/RGO/ITO	2.56×10^{-12}
APTES/MoO_3@RGO/ITO	8.06×10^{-12}
anti-HER-2/APTES/MoO_3@RGO/ITO	5.9×10^{-12}
BSA/anti-HER-2/APTES/MoO_3@RGO/ITO	4.3×10^{-12}

[a] $I_p = (2.69 \times 10^5) n^{3/2} A D^{1/2} C \nu^{1/2}$.

highest in the case of APTES/MoO_3@RGO/ITO, i.e., 8.06×10^{-12} $cm^2\ s^{-1}$, depicting the mesoporous behavior of MoO_3@RGO, due to the high aspect ratio of one-dimensional MoO_3 and the RGO substrate that promoted better electron conduction path from the electrolyte. However, after anti-HER-2 immobilization onto APTES/MoO_3@RGO surface, the D value decreased to 5.9×10^{-12} $cm^2\ s^{-1}$ and 4.3×10^{-12} $cm^2\ s^{-1}$ for BSA/anti-HER-2/APTES/MoO_3@RGO/ITO indicated the presence of anti-HER-2 and BSA that exhibited the insulating behavior which further slowed the diffusion process.[55] Further, the HET rate was determined from the EIS studies (Figure 8a). The HET was found to be the highest (3×10^{-7} cm s^{-1}) in case of the APTES/MoO_3@RGO/ITO with respect to APTES/MoO_3/ITO (1.9×10^{-7} cm s^{-1}) and APTES/RGO/ITO (2.3×10^{-7} cm s^{-1}) (see the Supporting Information).

Detection of Breast Cancer Biomarker. Under optimal conditions, BSA/anti-HER-2/APTES/MoO_3@RGO/ITO immunoelectrode was employed to detect the different levels of HER-2 using a three-electrode setup with PBS buffer (50 mM, 0.9% NaCl) containing $[Fe(CN)_6]^{3-/4-}$ (5 mM) (Figure 8b). It was observed that the observed anodic peak current decreased linearly with increasing concentration of HER-2 at a potential of 0.19 V. This decrease in current was attributed to the formation of the antigen−antibody complex layer at the APTES/MoO_3@RGO/ITO surface. At each concentration, the formed layer blocked the movement of electrons in and out of the surface leading to the hindered transport of generated electrons from the redox couple toward the electrode.

A calibration plot of the current values (mA) and the logarithm of HER-2 concentration (ng mL^{-1}) is shown in Figure 8c. All the experiments were repeated in triplicates at each concentration ($n = 3$). An excellent linear relation was obtained in the detection range (0.001−500 ng mL^{-1}) with the linear equation (eq 6)

$$I = 13.21\ \text{uA mL ng}^{-1}\text{cm}^{-2} + 1.30 \times 10^{-4} \log[\text{concentration of HER} - 2(\text{ng mL}^{-1})] \quad (6)$$

Further, the sensitivity of the fabricated immunoelectrode evaluated from the slope/surface area was found as 13 uA mL $ng^{-1}cm^{-2}$ with a regression coefficient of 0.98. The limit of detection of this immunosensor was calculated to be 0.00 1 ng mL^{-1}in solution using the standard equation (eq S3 in the Supporting Information). The magnitude of sensitivity improved and enhanced linear range was attributed to the mesoporic behavior due to the high surface area, as confirmed by BET studies) of the nanohybrid resulting in enhanced electronic and electrochemical properties. Here, the 2D substrate (RGO) that acted as efficient electron promoter (and 1D MoO_3 further increased the loading capacity of biomolecules that enhanced the chances of a greater antigen and antibody interactions.[56] The characteristic parameters of the MoO_3@RGO nanohybrid based HER-2 biosensor were compared with the other HER-2 based sensors[34] (Table 2). It may be noted that the MoO_3@RGO nanohybrid, when used as an immobilization matrix, exhibited a wider linear range and better LOD when compared with results reported in literature for other HER-2 biosensors including immunosensors, aptasensors, and sandwich assays.

Control and Selectivity Studies. The electrochemical response of the APTES/MoO_3@RGO/ITO electrode toward HER-2 as a control study was performed in the same range (0.001−500 ngmL^{-1}) under similar conditions (Figure 9a). The results revealed that no significant changes in the magnitude of the peak current were found toward increasing concentration of HER-2 suggesting that the sensor response was entirely due to the immunoreactions between antigens and antibodies only.[67] Further to investigate the cross-reactivity of the immunosensor, the sensor response toward the potential serum interferents such as CEA (4−16 ng mL^{-1}), glucose (10 mg mL^{-1}), CYFRA-21−1 (4 ng mL^{-1}), and cTnI (0.19 ng mL^{-1}) was determined considering their levels in serum (Figure 9b). The fabricated immunoelectrode was examined initially in the presence of 1 ng mL^{-1} of HER-2 (30 μL). Gradually, we introduced 30 μL each of glucose, cTnI, CYFRA-21−1and CEA one by one in the same solution and recorded the current response. The variation in the current response was found to be less than 5% in the presence of the potential interferents indicating good selectivity of the sensor. The selectivity coefficient coefficient for each interferent was determined to be ∼1 calculated using eq 9:

$$SC = \frac{I_c + i}{I_c} \quad (9)$$

Where Ic_{+I} is the current value of immunosensor in the presence of the interference and Ic in the absence exhibiting negligible change in the response.

Regeneration, Reproducibility, and Stability Studies. Regeneration of the fabricated immunosensor was evaluated after complete anti-HER-2 and HER-2 interaction (Figure S5a). This immunosensor was exposed to the drastic acidic/alkaline environment (p 2.5, DI and HCl for 90 s) followed by washing with PBS. The DPV peak response obtained after and before the regeneration (triplicates) exhibited a maximum change of 2.5% after fourth regeneration cycle and to 3.5% after the fifth cycle.

DOI: 10.1021/acsabm.9b00659
ACS Appl. Bio Mater. XXXX, XXX, XXX−XXX

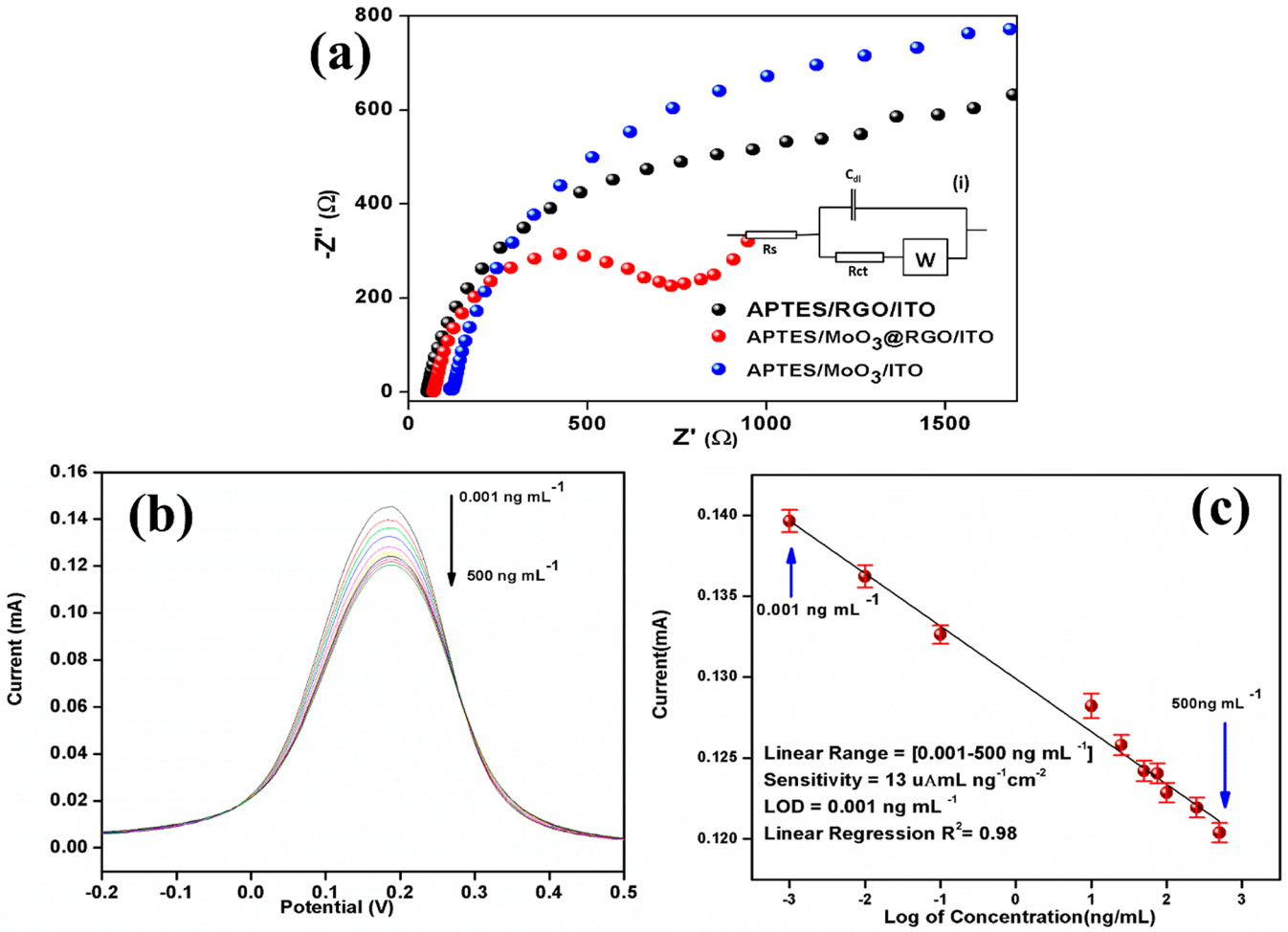

Figure 8. (a) EIS studies of APTES/RGO/ITO, APTES/MoO_3/ITO, and APTES/MoO_3@RGO/ITO (b) HER-2 sensing via DPV in the range (0.001−500 ng mL^{-1}), (c) calibration plot of log of HER-2 concentration vs current.

Table 2. Comparison of the Fabricated Immunosensor for Breast Cancer Detection with Existing Literature

bio analyte	detection techniques	label	linear detection range (ng mL^{-1})	limit of detection (ng mL^{-1})	sensitivity	response time (min)	refs
HER-2	surface acoustic wave	no	13−20				57
	electrochemical	yes	0−15		6 ng mL^{-1}	60	58
	field effect transistor based immunosensor.	no	6.86−68.6 × 10^{-3}	1.2 × 10^{-3}(% change/ mol)	0.1 ng mL^{-1}	40	59
	electrochemical	no	0.1 pg mL^{-1} to 10		1.117 ± 0.008 μA mL ng^{-1}	20	60
	sandwich immunoassay	yes	15−150	4.4			61
	electrochemical	no	10−110	7.4			62
	Non-Faradic impedance spectroscopy	no	0.2−2	6.0 × 10^{-3}			27
	Capacitive Aptasensor	no	0.2−2	0.2			63
	electrochemical aptasensor	no	0.5−2/2−75	0.22	0.14 μA mL ng^{-1}	60	33
	electrochemical	no	2.5−110	2.47	0.904 μA mL^{-1} ng cm^{-2}	20	29
	impedimetric	no	0.01−200	0.01	493.63 Ω ng^{-1} mL^{-1} cm^{-2}	15	64
	electrochemical sandwich immunoassay	yes	(5−20)/ (20−200)	4			65
	electrochemical aptasensor − sandwich assay	no	1−100	1		60	66
	electrochemical immunosensor	**no**	**0.001−500**	**0.001**	**13 μA mL^{-1} ng cm^{-2}**	**15**	**this work**

However, after the sixth cycle, only 85% of the current was retained. Thus, the developed immunosensor could be reutilized efficiently for 4 times only. Further,reproducibility was investigated by detecting HER-2 (1 ng mL^{-1}) using five different electrodes under similar conditions with the same surface area (Figure S5b). The relative standard deviation (% RSD) was calculated to be less than 10% stating a good precision and high reproducibility.

DOI: 10.1021/acsabm.9b00659
ACS Appl. Bio Mater. XXXX, XXX, XXX−XXX

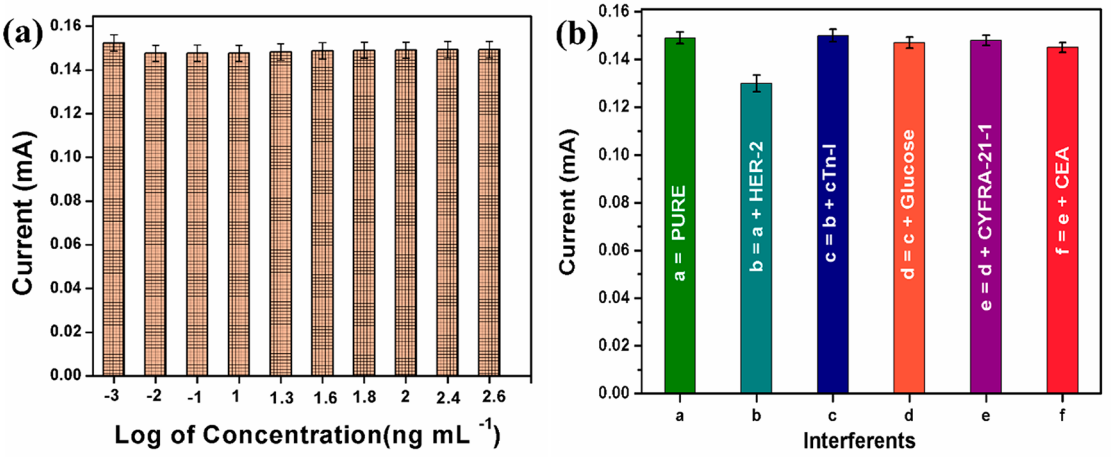

Figure 9. (a) Effect of HER-2 concentration on APTES/MoO_3@RGO/ITO (control study). (b) Effect of different interferents on BSA/anti-HER-2/APTES/MoO_3@RGO/ITO immunosensor.

Storage stability of the immunosesnors is a key factor for its commercial and clinical adaptability.The stability of the fabricated immunoelectrode was determined by DPV (BSA/anti-HER-2/APTES/MoO_3@RGO/ITO) at regular intervals for 10 weeks followed by storing at 4 °C when not in use (Figure S6). The results revealed that the immunosensor retained 98.5% of the biomolecular current response up to first 4 weeks, 94.8% of the activity until 9 weeks.Thereafter, the response degraded (~90%), indicating that immunosesnsor was stable for 9 weeks only, when kept at 4 °C.

Real Sample Analysis. The electrochemical response of the fabricated immunosensor (BSA/anti-HER-2/APTES/MoO3@RGO/ITO) toward the different concentration of serum ($n = 5$) samples was recorded (Figure S7) and correlated with those obtained using ELISA. A reasonable correlation was determined between the current obtained in both samples (standard and real) with an acceptable % RSD (Table S1). The results revealed that the developed immunosensor could significantly and accurately detect HER-2 in the clinical samples.

CONCLUSIONS

We have fabricated an efficient, rapid, label-free, sensitive immunosensor using a (MoO_3@RGO) nanohybrid platform for breast cancer detection. The 1D MoO_3 has been anchored on to the 2D substrate (RGO) via one-pot low-temperature hydrothermal synthesis and further functionalized using APTES. The specific surface area of this nanohybrid has been determined from BET analysis to be 2.58×10^2 m^2 g^{-1} with a pore size (8.4 nm) indicating the presence of mesoporous behavior with 14 folds enhancement of the surface area. The mesoporic behavior and increased functional groups (APTES/MoO_3@RGO) in this biosensor have resulted in excellent stability and reusability. This nanohybrid based sensor has shown improved parameters i.e higher diffusion coefficient; enhanced heterogeneous electron transfers and improved biomolecular loading resulting in broader linear detection range (0.001−500 ng mL^{-1}), better sensitivity (13 uA mL $ng^{-1}cm^{-2}$) and high selectivity. The remarkable lower limit of detection 0.001 ng mL^{-1} has revealed that this sensor can detect even minute concentration of HER-2 biomolecules. in the physiological range. This immunosensor may work as a diagnostic tool for monitoring of HER-2 with accuracy. Efforts should be made toward the application of this immune-electrode for detection of other potential biomarkers relating to diagnosis of the other diseases.

ASSOCIATED CONTENT

Supporting Information

The Supporting Information is available free of charge on the ACS Publications website at DOI: 10.1021/acsabm.9b00659.

Serum samples of breast cancer patients, Fourier transform infrared spectra (FT-IR) studies, scan rate studies, heterogeneous electron transfer rate (HET), survey scan spectrum, detection of breast cancer biomarker (HER-2) equation, regeneration and reproducibility studies, shelf life of the fabricated immunoelectrode, real sample analysis, Table S1 (PDF)

AUTHOR INFORMATION

Corresponding Author

*Email: bansi.malhotra@gmail.com.

ORCID

Bansi D. Malhotra: 0000-0002-0957-2684

Notes

The authors declare no competing financial interest.

ACKNOWLEDGMENTS

We are grateful to Prof. Yogesh Singh, Vice Chancellor, Delhi Technological University (DTU), Delhi, India, for providing the facilities. S.A. is thankful for the Senior Research Fellowship (SRF) award by CSIR, India [08/133/(0013)/2018-EMR-I]. B.D.M. thank the Science & Engineering Research Board (Government of India) for the award of a Distinguished Fellowship (SB/DF/011/2019). We thank Dr Prabhakar Rai and Prof Ashutosh Sharma, IIT Kanpur for the BET analysis. We also thank Dr. Birendra K. Yadav, Dr Anurag Mehta, Rajiv Gandhi Cancer Institute & Research Centre, Delhi, India, for the clinical samples.

REFERENCES

(1) Henrich, V. The Nature of Transition-Metal-Oxide Surfaces. *Prog. Surf. Sci.* **1983**, *14*, 175−199.

(2) Tan, C.; Zhang, H. J. C. S. R. Two-Dimensional Transition Metal Dichalcogenide Nanosheet-Based Composites. *Chem. Soc. Rev.* **2015**, *44*, 2713−2731.

DOI: 10.1021/acsabm.9b00659
ACS Appl. Bio Mater. XXXX, XXX, XXX−XXX

(3) Bai, S.; Chen, S.; Chen, L.; Zhang, K.; Luo, R.; Li, D.; Liu, C. C. Ultrasonic Synthesis of Moo3 Nanorods and Their Gas Sensing Properties. *Sens. Actuators, B* **2012**, *174*, 51−58.
(4) de Castro, I. A.; Datta, R. S.; Ou, J. Z.; Castellanos-Gomez, A.; Sriram, S.; Daeneke, T.; Kalantar-zadeh, K. Molybdenum Oxides−from Fundamentals to Functionality. *Adv. Mater.* **2017**, *29*, 1701619.
(5) Hu, B.; Mai, L.; Chen, W.; Yang, F. From Moo3 Nanobelts to Moo2 Nanorods: Structure Transformation and Electrical Transport. *ACS Nano* **2009**, *3*, 478−482.
(6) Li, H.; McRae, L.; Firby, C. J.; Al-Hussein, M.; Elezzabi, A. Y. Nanohybridization of Molybdenum Oxide with Tungsten Molybdenum Oxide Nanowires for Solution-Processed Fully Reversible Switching of Energy Storing Smart Windows. *Nano Energy* **2018**, *47*, 130−139.
(7) Balendhran, S.; Walia, S.; Nili, H.; Ou, J. Z.; Zhuiykov, S.; Kaner, R. B.; Sriram, S.; Bhaskaran, M.; Kalantar-zadeh, K. Two-Dimensional Molybdenum Trioxide and Dichalcogenides. *Adv. Funct. Mater.* **2013**, *23*, 3952−3970.
(8) Patzke, G. R.; Krumeich, F.; Nesper, R. Oxidic Nanotubes and Nanorods—Anisotropic Modules for a Future Nanotechnology. *Angew. Chem., Int. Ed.* **2002**, *41*, 2446−2461.
(9) Brezesinski, T.; Wang, J.; Tolbert, S. H.; Dunn, B. Ordered Mesoporous A-Moo 3 with Iso-Oriented Nanocrystalline Walls for Thin-Film Pseudocapacitors. *Nat. Mater.* **2010**, *9*, 146.
(10) Kolhar, P.; Anselmo, A. C.; Gupta, V.; Pant, K.; Prabhakarpandian, B.; Ruoslahti, E.; Mitragotri, S. Using Shape Effects to Target Antibody-Coated Nanoparticles to Lung and Brain Endothelium. *Proc. Natl. Acad. Sci. U. S. A.* **2013**, *110*, 10753−10758.
(11) Azizighannad, S.; Mitra, S. Stepwise Reduction of Graphene Oxide (Go) and Its Effects on Chemical and Colloidal Properties. *Sci. Rep.* **2018**, *8*, 10083.
(12) Hallfors, N.; Al Junaibi, S.; Liao, K.; Ismail, M.; Isakovic, A. Reduced Graphene Oxide for the Design of Electrocardiogram Sensors: Current Status and Perspectives. In *The Iot Physical Layer*; Springer: 2019; pp 3−11.
(13) Zhou, F.; Jing, W.; Xu, Y.; Chen, Z.; Jiang, Z.; Wei, Z. Performance Enhancement of Zno Nanorod-Based Enzymatic Glucose Sensor Via Reduced Graphene Oxide Deposition and Uv Irradiation. *Sens. Actuators, B* **2019**, *284*, 377−385.
(14) Oh, H.-J.; Jo, C.-H.; Yoon, C. S.; Yashiro, H.; Kim, S.-J.; Passerini, S.; Sun, Y.-K.; Myung, S.-T. Nickel Oxalate Dihydrate Nanorods Attached to Reduced Graphene Oxide Sheets as a High-Capacity Anode for Rechargeable Lithium Batteries. *NPG Asia Mater.* **2016**, *8*, 270.
(15) Verma, S.; Singh, A.; Shukla, A.; Kaswan, J.; Arora, K.; Ramirez-Vick, J.; Singh, P.; Singh, S. P. Anti-Il8/Aunps-Rgo/Ito as an Immunosensing Platform for Noninvasive Electrochemical Detection of Oral Cancer. *ACS Appl. Mater. Interfaces* **2017**, *9*, 27462−27474.
(16) Kumar, S.; Sharma, J. G.; Maji, S.; Malhotra, B. D. Nanostructured Zirconia Decorated Reduced Graphene Oxide Based Efficient Biosensing Platform for Non-Invasive Oral Cancer Detection. *Biosens. Bioelectron.* **2016**, *78*, 497−504.
(17) Ali, M. A.; Solanki, P. R.; Srivastava, S.; Singh, S.; Agrawal, V. V.; John, R.; Malhotra, B. D. Protein Functionalized Carbon Nanotubes-Based Smart Lab-on-a-Chip. *ACS Appl. Mater. Interfaces* **2015**, *7*, 5837−5846.
(18) Chen, Y.; Li, Y.; Deng, D.; He, H.; Yan, X.; Wang, Z.; Fan, C.; Luo, L. Effective Immobilization of Au Nanoparticles on Tio2 Loaded Graphene for a Novel Sandwich-Type Immunosensor. *Biosens. Bioelectron.* **2018**, *102*, 301−306.
(19) Li, Y.; Zhang, Z.; Zhang, Y.; Deng, D.; Luo, L.; Han, B.; Fan, C. Nitidine Chloride-Assisted Bio-Functionalization of Reduced Graphene Oxide by Bovine Serum Albumin for Impedimetric Immunosensing. *Biosens. Bioelectron.* **2016**, *79*, 536−542.
(20) Patil, S. B.; Udayabhanu, U.; Kishore, B.; Nagaraju, G.; Dupont, J. High Capacity Moo 3/Rgo Nanocomposite Anode for Lithium Ion Batteries: An Intuition into the Conversion Mechanism of Moo 3. *New J. Chem.* **2018**, *42*, 18569−18577.
(21) Devadoss, A.; Forsyth, R.; Bigham, R.; Abbasi, H.; Ali, M.; Tehrani, Z.; Liu, Y.; Guy, O. Ultrathin Functional Polymer Modified Graphene for Enhanced Enzymatic Electrochemical Sensing. *Biosensors* **2019**, *9*, 16.
(22) Weigel, M. T.; Dowsett, M. Current and Emerging Biomarkers in Breast Cancer: Prognosis and Prediction. *Endocr.-Relat. Cancer* **2010**, *17*, R245−R262.
(23) Nicolini, A.; Ferrari, P.; Duffy, M. J. In *Prognostic and Predictive Biomarkers in Breast Cancer: Past, Present and Future, Seminars in cancer biology*; Elsevier: 2018; pp 56−73.
(24) Narayan, T.; Kumar, S.; Kumar, S.; Augustine, S.; Yadav, B.; Malhotra, B. D. Protein Functionalised Self Assembled Monolayer Based Biosensor for Colon Cancer Detection. *Talanta* **2019**, *201*, 465−473.
(25) Gradishar, W. Her2 Therapy-an Abundance of Riches. *N. Engl. J. Med.* **2012**, *366*, 176−178.
(26) Larionov, A. A. Current Therapies for Human Epidermal Growth Factor Receptor 2-Positive Metastatic Breast Cancer Patients. *Front. Oncol.* **2018**, *8*, 89.
(27) Ravalli, A.; da Rocha, C. G.; Yamanaka, H.; Marrazza, G. A Label-Free Electrochemical Affisensor for Cancer Marker Detection: The Case of Her2. *Bioelectrochemistry* **2015**, *106*, 268−275.
(28) Eccles, S. A. The Role of C-Erbb-2/Her2/Neu in Breast Cancer Progression and Metastasis. *J. Journal of mammary gland biology neoplasia* **2001**, *6*, 393−406.
(29) Augustine, S.; Joshi, A. G.; Yadav, B. K.; Mehta, A.; Kumar, P.; Renugopalakrishanan, V.; Malhotra, B. D. An Emerging Nanostructured Molybdenum Trioxide-Based Biocompatible Sensor Platform for Breast Cancer Biomarker Detection. *MRS Commun.* **2018**, *8*, 668−679.
(30) Lai, L.-J.; Yang, Y.-W.; Lin, Y.-K.; Huang, L.-L.; Hsieh, Y.-H. Surface Characterization of Immunosensor Conjugated with Gold Nanoparticles Based on Cyclic Voltammetry and X-Ray Photoelectron Spectroscopy. *Colloids Surf., B* **2009**, *68*, 130−135.
(31) Freitas, M.; Nouws, H. P.; Delerue-Matos, C. Electrochemical Sensing Platforms for Her2-Ecd Breast Cancer Biomarker Detection. *Electroanalysis* **2019**, *31*, 121.
(32) Moelans, C.; De Weger, R.; Van der Wall, E.; Van Diest, P. Current Technologies for Her2 Testing in Breast Cancer. *J. Critical reviews in oncology/hematology* **2011**, *80*, 380−392.
(33) Tabasi, A.; Noorbakhsh, A.; Sharifi, E. Reduced Graphene Oxide-Chitosan-Aptamer Interface as New Platform for Ultrasensitive Detection of Human Epidermal Growth Factor Receptor 2. *Biosens. Bioelectron.* **2017**, *95*, 117−123.
(34) Patris, S.; De Pauw, P.; Vandeput, M.; Huet, J.; Van Antwerpen, P.; Muyldermans, S.; Kauffmann, J.-M. Nanoimmunoassay onto a Screen Printed Electrode for Her2 Breast Cancer Biomarker Determination. *Talanta* **2014**, *130*, 164−170.
(35) Emami, M.; Shamsipur, M.; Saber, R.; Irajirad, R. An Electrochemical Immunosensor for Detection of a Breast Cancer Biomarker Based on Antiher2−Iron Oxide Nanoparticle Bioconjugates. *Analyst* **2014**, *139*, 2858−2866.
(36) Luong, J. H.; Hrapovic, S.; Wang, D. Multiwall Carbon Nanotube (Mwcnt) Based Electrochemical Biosensors for Mediatorless Detection of Putrescine. *Electroanalysis* **2005**, *17*, 47−53.
(37) Srivastava, S.; Kumar, V.; Ali, M. A.; Solanki, P. R.; Srivastava, A.; Sumana, G.; Saxena, P. S.; Joshi, A. G.; Malhotra, B. Electrophoretically Deposited Reduced Graphene Oxide Platform for Food Toxin Detection. *Nanoscale* **2013**, *5*, 3043−3051.
(38) Arduini, F.; Giorgio, F. D.; Amine, A.; Cataldo, F.; Moscone, D.; Palleschi, G. Electroanalytical Characterization of Carbon Black Nanomaterial Paste Electrode: Development of Highly Sensitive Tyrosinase Biosensor for Catechol Detection. *Anal. Lett.* **2010**, *43*, 1688−1702.
(39) Khandare, L.; Late, D. J. Moo3-Rgo Nanocomposites for Electrochemical Energy Storage. *Appl. Surf. Sci.* **2017**, *418*, 2−8.
(40) Bai, S.; Chen, C.; Luo, R.; Chen, A.; Li, D. Synthesis of Moo3/Reduced Graphene Oxide Hybrids and Mechanism of Enhancing H2s Sensing Performances. *Sens. Actuators, B* **2015**, *216*, 113−120.

DOI: 10.1021/acsabm.9b00659
ACS Appl. Bio Mater. XXXX, XXX, XXX−XXX

(41) Xie, F.; Choy, W. C.; Wang, C.; Li, X.; Zhang, S.; Hou, J. Low-Temperature Solution-Processed Hydrogen Molybdenum and Vanadium Bronzes for an Efficient Hole-Transport Layer in Organic Electronics. *Adv. Mater.* **2013**, *25*, 2051−2055.
(42) Liu, Y.; Li, Y.; Li, X.-M.; He, T. Kinetics of (3-Aminopropyl) Triethoxylsilane (Aptes) Silanization of Superparamagnetic Iron Oxide Nanoparticles. *Langmuir* **2013**, *29*, 15275−15282.
(43) Dupin, J.-C.; Gonbeau, D.; Vinatier, P.; Levasseur, A. Systematic Xps Studies of Metal Oxides, Hydroxides and Peroxides. *Phys. Chem. Chem. Phys.* **2000**, *2*, 1319−1324.
(44) Reverberi, R.; Reverberi, L. Factors Affecting the Antigen-Antibody Reaction. *Blood Transfus.* **2007**, *5*, 227−240.
(45) Kumar, S.; Lei, Y.; Alshareef, N. H.; Quevedo-Lopez, M.; Salama, K. N. Biofunctionalized Two-Dimensional Ti3c2Mxenes for Ultrasensitive Detection of Cancer Biomarker. *Biosens. Bioelectron.* **2018**, *121*, 243−249.
(46) Bard, A. J.; Faulkner, L. R.; Leddy, J.; Zoski, C. G. *Electrochemical Methods: Fundamentals and Applications*; Wiley: New York, 1980; Vol. 2.
(47) Yuan, Y.; Li, L.; Zhao, M.; Zhou, J.; Chen, Z.; Bai, L. An Aptamer Based Voltammetric Biosensor for Endotoxins Using a Functionalized Graphene and Molybdenum Disulfide Composite as a New Nanocarrier. *Analyst* **2019**, *144*, 1253.
(48) Solanki, P. R.; Kaushik, A.; Ansari, A. A.; Tiwari, A.; Malhotra, B. J. S.; Chemical, A. B. *Sens. Actuators, B* **2009**, *137*, 727−735.
(49) Mondal, K.; Ali, M. A.; Singh, C.; Sumana, G.; Malhotra, B. D.; Sharma, A. Highly Sensitive Porous Carbon and Metal/Carbon Conducting Nanofiber Based Enzymatic Biosensors for Triglyceride Detection. *Sens. Actuators, B* **2017**, *246*, 202−214.
(50) Xiao, J.; Yang, S. Bio-Inspired Synthesis of Nacl-Type Co X Ni 1− X O (0≤ X< 1) Nanorods on Reduced Graphene Oxide Sheets and Screening for Asymmetric Electrochemical Capacitors. *J. Mater. Chem.* **2012**, *22*, 12253−12262.
(51) Zhou, M.; Zhai, Y.; Dong, S. Electrochemical Sensing and Biosensing Platform Based on Chemically Reduced Graphene Oxide. *Anal. Chem.* **2009**, *81*, 5603−5613.
(52) Huang, W.; Ding, S.; Chen, Y.; Hao, W.; Lai, X.; Peng, J.; Tu, J.; Cao, Y.; Li, X. 3d Nio Hollow Sphere/Reduced Graphene Oxide Composite for High-Performance Glucose Biosensor. *Sci. Rep.* **2017**, *7*, 5220.
(53) Aydın, E. B.; Sezgintürk, M. K. A Sensitive and Disposable Electrochemical Immunosensor for Detection of Sox2, a Biomarker of Cancer. *Talanta* **2017**, *172*, 162−170.
(54) Singh, R.; Hong, S.; Jang, J. Label-Free Detection of Influenza Viruses Using a Reduced Graphene Oxide-Based Electrochemical Immunosensor Integrated with a Microfluidic Platform. *Sci. Rep.* **2017**, *7*, 42771.
(55) Ali, M. A.; Srivastava, S.; Mondal, K.; Chavhan, P. M.; Agrawal, V. V.; John, R.; Sharma, A.; Malhotra, B. D. A Surface Functionalized Nanoporous Titania Integrated Microfluidic Biochip. *Nanoscale* **2014**, *6*, 13958−13969.
(56) Ali, M. A.; Srivastava, S.; Agrawal, V. V.; Willander, M.; John, R.; Malhotra, B. D. A Biofunctionalized Quantum Dot−Nickel Oxide Nanorod Based Smart Platform for Lipid Detection. *J. Mater. Chem. B* **2016**, *4*, 2706−2714.
(57) Gruhl, F. J.; Rapp, M.; Länge, K. Label-Free Detection of Breast Cancer Marker Her-2/Neu with an Acoustic Biosensor. *Procedia Eng.* **2010**, *5*, 914−917.
(58) Al-Khafaji, Q.; Tombelli, S.; Laschi, S.; Marrazza, G.; Mascini, M.; Mohammed, N. Detection of a Tumor Marker in Serum by an Electrochemical Assay Coupled to Magnetic Beads. In *Sensors and Microsystems*; Springer: 2011; pp 157−161.
(59) Myung, S.; Solanki, A.; Kim, C.; Park, J.; Kim, K. S.; Lee, K. B. Graphene-Encapsulated Nanoparticle-Based Biosensor for the Selective Detection of Cancer Biomarkers. *Adv. Mater.* **2011**, *23*, 2221−2225.
(60) Zhu, Y.; Chandra, P.; Shim, Y.-B. Ultrasensitive and Selective Electrochemical Diagnosis of Breast Cancer Based on a Hydrazine−Au Nanoparticle−Aptamer Bioconjugate. *Anal. Chem.* **2013**, *85*, 1058−1064.
(61) Marques, R. C.; Viswanathan, S.; Nouws, H. P.; Delerue-Matos, C.; González-García, M. B. Electrochemical Immunosensor for the Analysis of the Breast Cancer Biomarker Her2 Ecd. *Talanta* **2014**, *129*, 594−599.
(62) Arkan, E.; Saber, R.; Karimi, Z.; Shamsipur, M. A Novel Antibody−Antigen Based Impedimetric Immunosensor for Low Level Detection of Her2 in Serum Samples of Breast Cancer Patients Via Modification of a Gold Nanoparticles Decorated Multiwall Carbon Nanotube-Ionic Liquid Electrode. *Anal. Chim. Acta* **2015**, *874*, 66−74.
(63) Qureshi, A.; Gurbuz, Y.; Niazi, J. H. Label-Free Capacitance Based Aptasensor Platform for the Detection of Her2/Erbb2 Cancer Biomarker in Serum. *Sens. Actuators, B* **2015**, *220*, 1145−1151.
(64) Sharma, S.; Zapatero-Rodríguez, J.; Saxena, R.; O'Kennedy, R.; Srivastava, S. Ultrasensitive Direct Impedimetric Immunosensor for Detection of Serum Her2. *Biosens. Bioelectron.* **2018**, *106*, 78−85.
(65) Tallapragada, S. D.; Layek, K.; Mukherjee, R.; Mistry, K. K.; Ghosh, M. Development of Screen-Printed Electrode Based Immunosensor for the Detection of Her2 Antigen in Human Serum Samples. *Bioelectrochemistry* **2017**, *118*, 25−30.
(66) Jarczewska, M.; Trojan, A.; Gągała, M.; Malinowska, E. Studies on the Affinity-Based Biosensors for Electrochemical Detection of Her2 Cancer Biomarker. *Electroanalysis* **2019**, *31*, 1125.
(67) Yu, Y.; Huang, Z.; Zhou, Y.; Zhang, L.; Liu, A.; Chen, W.; Lin, J.; Peng, H. J. B. Facile and Highly Sensitive Photoelectrochemical Biosensing Platform Based on Hierarchical Architectured Polydopamine/Tungsten Oxide Nanocomposite Film. *Biosens. Bioelectron.* **2019**, *126*, 1−6.

DOI: 10.1021/acsabm.9b00659
ACS Appl. Bio Mater. XXXX, XXX, XXX−XXX